STAR FORMATION HISTORIES OF CLUSTER GALAXIES

David Pérez-Millán
Examen de Candidatura a Doctorado
IRyA, UNAM

1 Introduction

It is now a known fact that the environment plays an important role in galaxy evolution. Observations of galaxies in local clusters, in the field, and in distant clusters, have different features, reflecting their different evolutionary paths. In the local universe, late-type galaxies dominate the low-density environments, while early-type galaxies are preferentially found in dense environments like cluster cores (Dressler, 1980). Nevertheless, this segregation of galaxies could be a mass-dependent effect, as late-types have preferentially low masses, (Wuyts et al., 2011), and there are more low-mass galaxies in low-density environments (Kauffmann et al., 2004).
High-redshift galaxy clusters are instead characterized by a population of blue, star-forming spiral galaxies which is almost absent in the local universe (Butcher and Oemler, 1978, 1984). While the fraction of ellipticals remains more or less uniform since $z \sim 1$, at this same redshift the S0 population is observed to be scarce (Desai et al., 2007). These are some of the most striking examples of evolutionary effects taking place in galaxies within dense environments. Other high-redshift studies have revealed that a particular morphological mix depends on the global cluster properties, in particular on X-ray luminosity and velocity dispersion, both considered good tracers of the cluster mass (Postman et al., 2005). To perform a comparison between high- and low-redshift cluster galaxies, and study the relation between morphological variations and global environment, we need to quantify the morphological evolution as a function of cluster mass.
Galaxies are likely to have their star-formation activity quenched if they are massive, or located in dense environments (Kauffmann et al., 2003). The vast majority of quenched galaxies have early types, suggesting that morphological type and quenching of star formation could be related. Schawinski et al. (2014) studied the relation between morphology and star formation histories (SFHs) in low-redshift galaxies and found two evolutionary pathways towards quenching: the slow quenching of late types through secular evolution, and the fast quenching of early types with star formation, probably driven by major mergers. A third pathway could be due to weaker interactions, causing an intermediate quenching (Smethurst et al., 2015). Other studies (e.g., Liu et al., 2015) have also suggested that the environment may not be the fundamental parameter in the quenching of star formation, and that both morphological transformation and quenching of star formation are mainly driven by stellar mass for massive galaxies (Liu et al., 2019).

1.1 Physical processes affecting galaxy evolution in clusters

Galaxy clusters are the most massive quasi-equilibrium systems in the Universe. They are peaks of density in the galaxy distribution and can be used to probe a broad range of physical conditions, from the dense cores to the outermost low-density regions. They provide large samples of galaxies at the same redshift in a relatively small observable field. Only in clusters, we can observe directly

the interaction between galaxies and the intergalactic medium and, due to the physical proximity of galaxies, we can study the striking differences between cluster and field populations. As a consequence, galaxy clusters represent fundamental places to trace the evolution of themselves, as well as that of their galaxies, and to investigate the effects of the environment on galaxy evolution. By galaxy evolution, we refer to the changes across time in the stellar population properties, interstellar medium (ISM) content, and morphologies. This evolution can be driven both by internal and external physical mechanisms. Internal mechanisms include several astrophysical processes, such as star formation activity, the most important one among those related to stellar evolution (Kennicutt, 1998), like supernovae explosions (Burrows, 2000); nuclear activity, in particular, accretion phenomena onto a supermassive black hole, and the related release of mechanical and electromagnetic energy (Silk and Rees, 1998); the structural configuration of the different morphological components, e.g., angular momentum reconfiguration by stellar bars (Debattista and Sellwood, 2000). External mechanisms playing a major role include the influence of the gravitational potential of the cluster, galaxy-galaxy interactions, and interactions between galaxies and the hot and low-density gas of the intracluster medium (ICM; see e.g., Boselli and Gavazzi, 2006).
Several of such environmental-dependent processes have been identified and proposed to explain the different evolutionary paths that galaxies in clusters follow compared to isolated ones, regarding their stellar content, their SFH, and their morphology. These processes include: harassment, that consists in repeated high velocity encounters with galaxies in the cluster (Moore et al., 1996); starvation or strangulation, which is the removal of the galactic gas halo, which fuels star formation during cluster collapse (Larson et al., 1980); ram-pressure stripping, i.e., the removal of the cold interstellar gas through high-velocity interactions with the ICM (Gunn and Gott, 1972); thermal evaporation (Cowie and Songaila, 1977); major and minor mergers (Toomre, 1977); and the overall tidal influence of the cluster (Byrd and Valtonen, 1990).
Environment influences not only the morphology of galaxies, but also their gas content; since the SFH of a galaxy crucially depends on the amount of gas available, any process removing, adding, or even perturbing the gas is ultimately determining the evolution and the fate of a galaxy, at least as far as the stellar content is concerned. It is still debated whether the environment affects the whole SFH or only at some moment of the galaxy's life, leading to quenching. This interdependence morphology/star formation/environment complicates disentangling the processes affecting galaxy components and evolution.

1.2 Open questions

One of the main challenges that modern extragalactic astrophysics faces is understanding the different mechanisms driving the changes in galactic properties. While isolated galaxies follow evolutionary paths and timescales that are mostly driven by the typical processes of stellar evolution, galaxies in clusters are subject to a whole range of different processes and interactions that dramatically change that picture. This is reflected in the differences of the galaxy population of clusters vis-a-vis that of the field, from the galactic color-magnitude diagram to the morphology-density relation, and the luminosity function. If a galaxy enters a cluster, its evolution receives a kick that accelerates changes in its stellar and ISM contents. What are the processes, among those mentioned above, that are the main drivers of these changes? Which galactic components and properties do they affect the most? Under which conditions is one dominating over the others? What are the prevailing effects: those from the global environment or those of the local one? These are some of the most urgent questions in the extragalactic astrophysics and they are also one of the main drivers for the development of upcoming and future instruments and space missions.

The relation between the local density and the stellar mass distribution of galaxies in clusters and field galaxies was studied by Vulcani et al. (2012), who found that at least at $z \leq 0.8$, local density is more important than global environment in the stellar mass distribution of galaxies, suggesting that galaxy properties are more strongly dependent on local processes. Cava et al. (2017) analyzed a large sample of galaxies in clusters, obtaining that spiral galaxies are a recently accreted population to clusters. During the accretion, spirals change their phase-space distribution, approaching that of cluster ellipticals; it would take them ≤ 3 Gyr to evolve into S0 galaxies. This process is nowadays mainly completed in regular clusters, but still ongoing in nearby irregular clusters. A study of the SFHs of S0 galaxies in regular and irregular clusters could provide interesting hints on the connection between S0 and spiral galaxies, and the timescale for this transformation.
Fraser-McKelvie et al. (2018a) used data from the survey called Mapping Nearby Galaxies at Apache Point Observatory (MaNGA; Bundy et al., 2015) to study the formation mechanisms of S0 galaxies, and found that there are two main channels: low-mass S0s are formed through the disappearance of the disk of a spiral galaxy, more precisely because of hydrodynamical effects; while high-mass S0s are most likely produced by other mechanisms (or a combination of them), such as galaxy mergers. These results are in a way similar to those obtained by Fraser-McKelvie et al. (2018b) for a sample of passive spirals, studying the dominant quenching mechanisms. They conclude that low-mass spirals are quenched due to gas stripping and heating processes operating in rich clusters. High-mass passive spirals are present mostly, but not exclusively, in groups, and there is evidence for both internal and environmental quenching or neither. In conclusion, it is argued that there is no privileged mechanism to quench star formation in high-mass spiral galaxies, but a mixture of all processes.
Contini et al. (2019), using an analytic model of galaxy formation, found that, for $z \leq 1.5$, the star formation rate (SFR) and the specific SFR (sSFR) are independent of the environment, but both SFR and sSFR are strongly dependent on stellar mass. This seems at odds with the findings of Guglielmo et al. (2015), who claim that the average SFH of a galaxy depends on its mass but, at fixed mass, the SFH depends on the environment and is almost independent of present morphology.
The determination of the morphological fraction of galaxies as a function of local density is still based on the historical database of Dressler (1980), who used photographic plates for galaxies in 55 clusters in the range of $0.011 \leq z \leq 0.066$. This complex task can now be undertaken using wide-field cameras to map a large number of clusters at low redshift. Leveraging current facilities, in this work we exploit the largest, most complete, and most homogeneous database of cluster galaxies of the local universe, and attempt to take further steps towards an answer to some of the questions currently puzzling the astronomical community on galaxy evolution. These questions are: is the environment or galaxy stellar mass the most important factor for the quenching of star formation in galaxies? Which mechanisms are the most important for galaxies lose their gas during the accretion into clusters? How are these processes related to the relaxation of the dynamical state of the cluster? Is the present-day SFR related to the cluster state of evolution? What about the SFH? What makes the environment suitable to have high-mass red spirals? Could we say something about the morphological transformation of spiral into S0s?
In this work, we assume a ΛCDM cosmological model with $\Omega_{\rm m} = 0.3$, $\Omega_\Lambda = 0.7$, and $H_0 = 70$ km s^{-1} Mpc^{-1}. Furthermore we assume, whenever necessary, a Chabrier (2003) initial mass function (IMF).

2 Dataset

The WIde-field Nearby Galaxy-cluster Survey (WINGS; Fasano et al., 2006) is a targeted survey of a sample of galaxy clusters selected from the ROentgen SATellite (ROSAT) Brightest Cluster Sample (BCS; Ebeling et al., 1998), and its extension (eBCS; Ebeling et al., 2000) in the northern hemisphere, and the X-ray Brightest Abell-type cluster sample (XBACs; Ebeling et al., 1996) in the southern hemisphere. WINGS was conceived to provide a complete and homogeneous observational dataset, to allow a systematic study of the environment, cluster properties, as well as of the galaxies in them, in a low redshift ($0.04 < z < 0.07$) cluster sample. The sample may serve as a reference for subsequent studies at higher redshifts and evolutionary studies. Initially, WINGS was an optical and spectroscopic survey of galaxies located toward the center of clusters, but it was then extended to cover a larger area, through the survey known as OmegaWINGS.

The WINGS cluster sample covers both a full range in X-ray luminosity ($\log L_X[0.1 - 2.4 \text{ keV}] = 43.2 - 44.7$) and a wide range in velocity dispersion ($\sigma_{\rm cl} \sim 400 - 1400$ km s^{-1}). The catalog is uncontaminated by non-clusters X-ray sources, like AGNs or foreground stars. The clusters were selected with a high galactic latitude ($|b| > 20^\circ$), and the low redshift range was chosen to guarantee both a good spatial resolution ($1'' \leq 1.3$ kpc) and a large observed field ($34' \geq 1.6$ Mpc). A full description of the cluster sample can be looked up in Fasano et al. (2006).

The original WINGS sample contains 77 clusters (41 in the southern hemisphere and 36 in the northern hemisphere), selected to cover a full mass range of local clusters. There was the initial intent of obtaining spectroscopic observations for all clusters, but due to bad weather conditions, especially in the north, this was not possible. Table 3 (see Appendix A) lists the WINGS cluster sample with some basic properties.

2.1 WINGS: photometric and spectroscopic survey

The first part of the WINGS survey is called WINGS-OPT (Varela et al., 2009). It consists in the optical B and V imaging survey of fields size $\sim 35' \times 35'$ of objects in the cluster sample, using the wide-field cameras on the 2.5 m Isaac Newton Telescope (INT/WFC) for the northern clusters, and the MPG/ESO-2.2 m telescope (ESO/WFI) for the southern clusters. The pixel scale is 0.333 arcsec/pix for the INT images, and 0.238 arcsec/pix for the WFI images. The construction of the mosaic images is described in Fasano et al. (2006), and the image description is found in Varela et al. (2009).

WINGS-SPE (Cava et al., 2009) is a multi-fiber, medium-resolution survey for a subsample of the WINGS-OPT sample. For the northern clusters was used the AF2/WYFFOS multifiber spectrograph mounted on the 4.2 m William Herschel Telescope (WHT). The southern clusters were observed with the 2dF multifiber spectrograph on the 3.9 m Anglo Australian Telescope (AAT). With the AF2/WYFFOS 60-70 objects can be observed with one fiber each, while the 2dF can observe up to 400 objects simultaneously with its two-degree field of view (FoV).

As mentioned before, bad weather prevented the acquisition of spectroscopic data for the whole sample, especially in the north, where 25% of observing time was lost. The priority, then, was to observe those clusters with few (< 20) or no redshifts available from the literature. Despite these problems, the spectroscopic sample provides information of redshifts and memberships for 48 clusters (22 in the southern sky and 26 in the northern sky; see subsection 3.2), with $\sim 30\%$ overlap with previously published datasets, such as the 2dF Galaxy Redshift (2dFGRS; Colless et al., 2001) and the Sloan Digital Sky (SDSS; Strauss et al., 2002). The SDSS only has 12 clusters in common with WINGS-SPE.

2.2 OmegaWINGS: photometric and spectroscopic survey

WINGS is a unique dataset for studying cluster galaxies in great detail, but it is limited to the cluster cores ($R < 0.6 \times R_{200}$ for all clusters). Given that the outer regions of clusters are ideal sites for studying and understanding the dynamics and transformations galaxies undergo as they are falling towards the cluster center, and that, the region between clusters and the surrounding field has been poorly studied, the original WINGS survey was extended to cover at least up to one virial radius and in some cases two virial radii and beyond, for a subsample of the WINGS clusters. This new dataset is known as OmegaWINGS (Gullieuszik et al., 2015), providing us a more homogeneous and detailed study, much more than the SDSS.

OmegaWINGS covers a field of 1 deg^2 in photometry for each of 46 WINGS clusters in 45 fields, randomly selected from the 57 clusters that can be observed from the Very Large Telescope (VLT) Survey Telescope (VST; $\delta < 20$ deg). The B and V imaging was made with the OmegaCAM (hence the name OmegaWINGS) at the 2.6 m VST, with a plate scale of 0.21 arcsec/pix (see Gullieuszik et al., 2015 for more observation details).

For the OmegaWINGS spectroscopic survey (Moretti et al., 2017), 33 of the 46 clusters observed with VST were selected, including 12 clusters that have not been observed in WINGS-SPE. The galaxy sample was chosen using the OmegaWINGS photometric catalogs. Galaxies brighter than $V = 20$ mag were selected and divided in two groups: bright ($V_{\rm fib} \leq 20.5$ mag) and faint ($20.5 < V_{\rm fib} \leq 21.5$ mag) sources. Bright sources were observed for 60 minutes, and faint sources for 120 minutes. To exclude background galaxies, a color limit very close to $B-V = 1.20$ mag was applied, depending on the cluster. Finally, a priority was assigned to the targets, with the highest one for those galaxies located outside the original WINGS fields, then for objects in the WINGS area but without a spectrum, and the lowest priority for targets located in the WINGS regions with a measured redshift.

2.3 Spectra

The spectra cover the range $\sim 3800 - 7000$ Å with a resolution FWHM $= 3 - 6$ Å and a fiber aperture of $1.''6$. For the southern sky, we used all the 22 clusters observed in WINGS-SPE; they have a resolution of FWHM $= 9$ Å, a wavelength range of $3600 - 8000$ Å, and a fiber diameter of $2''$. OmegaWINGS spectra all have a good quality, with a resolution of FWHM $= 3.5 - 6$ Å, and a fiber diameter of $2.''16$.

After checking the quality of WINGS spectra taken with the WHT (in the northern sky), we decided to only use the galaxy spectra for 7 clusters (A376, A1795, A1983, A2457, A2626, Z8338, and Z8852), which have the best signal-to-noise ratio (SNR). In this work, we utilized 6645 galaxies in OmegaWINGS and 2797 galaxies in WINGS, with a total of 33 clusters. Considering that some galaxies were observed in both spectroscopic surveys, the total number of distinct galaxies with spectra is 8626.

2.4 Completeness

Not all galaxies detected in the images (see subsection 3.1) have a spectroscopic counterpart, because of two reasons: the number of fibers in the spectrometers is limited and, due to the physical size of the fibers, they cannot overlap to cover the densest part of clusters, typically towards the center, where the highest number of galaxies is located. The second reason is that brighter galaxies are more easily observed, in special, because of the observing time is limited. Neglecting these two facts might lead to wrong conclusions when analyzing the occurrence and the properties of galaxies as a function of their luminosity and (projected) position in the cluster.

These two considerations carry to the magnitude completeness $C(m)$ and the radial (geometrical) completeness $C(r)$, respectively (see Cava et al., 2009, for details).
This is why we need to take into account these two limitations of the survey, and we do this by using the spectroscopic completeness, i.e., by weighing, when necessary, the properties of each galaxy with:

$$W(m,r) = \frac{1}{C(m) \times C(r)}. \quad (1)$$

3 Previous results

Here we use some results previously obtained for the WINGS and OmegaWINGS datasets. These include photometry, membership of galaxies in clusters, morphological classification, projected clustercentric distances, and local density.

3.1 Photometry

Source extraction and photometry were performed using SExtractor (Bertin and Arnouts, 1996), with a detection threshold of 1.5σ above the background. The final number of objects includes only those detected in both bands. For WINGS, the photometric catalog comprises ~ 394280 galaxies, 90% complete at $V \sim 21.7$ and 50% at $V \sim 23.2$ in general (Varela et al., 2009). For OmegaWINGS 195756 objects were classified as galaxies, with a completeness of 80% at $V = 22.4$ and 50% at $V = 23.1$ (Gullieuszik et al., 2015). The astrometry accuracy is $\sim 0.''2$ for WINGS and at least $0.''1$ for OmegaWINGS, compared to typical dispersion of $0.''2$ for 2MASS, and $0.''07$ for SDSS. The photometric catalogs list parameters such as WINGS unique ID, sky coordinates, host cluster, flag (star, galaxy or unknown), axial ratio, and B and V total and aperture magnitudes.

3.2 Redshift and membership

The galaxies targeted with spectroscopy were selected to have a total magnitude $V < 20$, a magnitude within the fiber aperture $V_{\rm fib} < 21.5$ or fainter in a few cases, and a color of $(B-V)_{5\ \rm kpc} \lesssim 1.4$ within a 5 kpc aperture, with small variations depending on the cluster. These magnitudes and colors have been corrected by extinction by dust in the Milky Way, and the selection limits were applied to avoid any bias in the observed galaxy type, as occurs when choices are made based on the color-magnitude diagram only (which mainly selects red galaxies). As for the redshift measurements, they were performed by Cava et al. (2009) for WINGS and Moretti et al. (2017) for OmegaWINGS. A semi-automatic method was used, based on the IRAF/XCSAO task; this task identifies emission lines and cross-correlates the spectrum with a zero velocity template. Members of the WINGS team visually inspected every single spectrum to ensure the automatic result was correct. Additionally, each measurement was corrected to the heliocentric velocity. The typical error in radial velocities is ~ 25 km s^{-1}.
For WINGS, 6132 redshifts were obtained, of which 3694 were tagged as cluster members; for OmegaWINGS 17985 redshifts were measured and the number of cluster members is 10229. There are four clusters in OmegaWINGS (A1069, A2382, A3158, and A4059) that have a second group of galaxies outside the main group (with radial velocities ± 3 times the velocity dispersion of the cluster). In these cases, such galaxies were also included as cluster members, being part of a second structure falling towards the main group.

3.3 Cluster velocity dispersion

An iterative $\pm 3\sigma$ clipping algorithm (Beers et al., 1990) was adopted to determine cluster membership, and thereby obtain the cluster velocity dispersion, on average, with up to three times member galaxies than previous studies for WINGS clusters (e.g., SDSS). The velocity dispersion values span a range of $\sigma \simeq 400 - 1300$ km s^{-1} (see Table 3 in Appendix A).
We took R_{200} as the cluster virial radius. This is the radius at which the enclosed mean mass density exceeds the critical density of the Universe by a factor of 200 (Peebles, 1993). From the cluster radial velocity ($\sigma_{\rm cl}$) and the (mean) cluster redshift ($z_{\rm cl}$), following Poggianti et al. (2006), R_{200} is calculated as:

$$R_{200} = 1.73 \, \frac{\sigma_{\rm cl}}{1000 \text{ km s}^{-1}} \frac{1}{\sqrt{\Omega_\Lambda + \Omega_0 (1+z_{\rm cl})^3}} \, h^{-1} \text{ Mpc.} \quad (2)$$

WINGS clusters fields were chosen to observe at least up to $0.6 \times R_{200}$, while OmegaWINGS fields allow reaching at least the virial radius, and for some cases even out to $2 \times R_{200}$, where there still exist cluster members.

3.4 Morphology

The morphological classification of cluster galaxies was one of the most important goals of the WINGS survey. To achieve this, the `MORPHOT` (Fasano et al., 2012) tool was developed, and applied to the V-band images. `MORPHOT` provides two independent methods to classify galaxies, one based on the maximum likelihood, another on a neural network machine. The final classification is a combination of these two techniques, which proves to be effective in a comparison with ~ 1000 galaxies from the SDSS. Additionally, a sample of ~ 3000 galaxies randomly selected from WINGS was classified visually, and compared with `MORPHOT`, with agreement results. `MORPHOT` can differentiate between elliptical and lenticular galaxies with unprecedented accuracy, and uses a slightly modified version of the Revised Hubble Type ($T_{\rm RH}$), denoted by $T_{\rm M}$ (`MORPHOT` type), as indicated in Table 1; $T_{\rm M}$ maps galaxy type as follows:

- Ellipticals (E): $-6 \leq T_M < -4$
- Lenticulars (S0): $-4 \leq T_M \leq 0$
- Early spirals (SpE): $0 < T_M \leq 4$
- Late spirals and Irregulars (SpL): $4 < T_M \leq 11$

In several cases, we only use the three main types: ellipticals, lenticulars and spirals, in which we refer to spiral galaxies for those with types $0 < T_M \leq 11$. The morphological classification is provided for 39923 galaxies in WINGS (Fasano et al., 2012), and for 49883 galaxies in OmegaWINGS (A. Moretti, private communication, February 2019).

-6	-5	-4	-3	-2	-1	0	1	2	3	4	5	6	7	8	9	10	11
cD	E	E/S0	S0$^-$	S0	S0$^+$	S0/a	Sa	Sab	Sb	Sbc	Sc	Scd	Sd	Sdm	Sm	Im	cIrr

Table 1: Morphological classification given by the MORPHOT tool.

3.5 Clustercentric (projected) distance

We analyzed several properties of galaxies as a function of their projected distances to the cluster center, in which we considered two different centers: the brightest cluster galaxy (BCG), and the maximum intensity of the X-ray emission. For most WINGS clusters, these two positions are the same, but 13/77 WINGS clusters have two BCGs. Thus, we took as cluster center the optical position of the peak in the X-ray emission, updated by Biviano et al. (2017). Clustercentric distance, from spherical trigonometry, is given by:

$$\theta = \cos^{-1}\left[\sin\delta_g \sin\delta_c + \cos\delta_g \cos\delta_c \cos(\alpha_g - \alpha_c)\right], \tag{3}$$

with the subscripts g for galaxy, and c for the cluster center. Then, using the cluster redshifts, this projected distance is converted into a linear distance, in units of the virial radius, for each cluster (R_{200} updated by Biviano et al., 2017).

3.6 Local density

Galaxy density has an important role in studying many galaxy properties, such as SFR, morphology, color, and gas content. To study physical processes in galaxy evolution in several environments, we take advantage of the local density obtained by Vulcani et al. (2012) for WINGS and OmegaWINGS (A. Moretti, private communication, October 2019). The projected local density is defined as:

$$\Sigma = \frac{N}{A}, \tag{4}$$

calculated from the circular area $A = \pi R_N^2$ (Mpc^2) in the sky, enclosing the N nearest projected neighbors brighter than certain limit in absolute V magnitude (in this case, $M_V = -19.5$), applying a correction for spectroscopic incompleteness. For the high galaxy densities found in clusters, N is taken as 10, while for the field N can be 5 (Baldry et al., 2004). Thus, for each cluster member galaxy A_{10}, enclosing the 10 nearest projected galaxies, was computed. Given the lack of spectroscopy for all galaxies, a limit in M_V was imposed to eliminate background galaxies, as well as an additional statistical correction to account for field galaxies contamination (see details in Vulcani et al., 2012).

4 The SINOPSIS code

The WINGS project also aimed to study galaxy populations in clusters and the influence of the environment on the physical properties of galaxies. For this purpose, a stellar population synthesis code was developed, based on previous work by Poggianti et al. (2001) produced to derive SFHs. Here we will briefly describe `SINOPSIS`[1] (SImulatiNg OPtical Spectra wIth Stellar population models; Fritz et al., 2007, 2011) and its results. `SINOPSIS` is a spectrophotometric fitting code that can recover the characteristics of the stellar populations of galaxies, such as their SFR, SFH, mean stellar ages, stellar mass, dust extinction, among others.

4.1 The code

`SINOPSIS` aims to reconstruct the SFH of galaxies, by reproducing the main features of the observed spectrum: the equivalent width (EW) of the most significant emission and absorption lines: Hα, Hβ, Hδ, Hϵ+CaII (H), CaII (K), Hη, and [OII] (Fritz et al., 2007), and the continuum flux, measured

[1] `http://www.irya.unam.mx/gente/j.fritz/JFhp/SINOPSIS.html`

in particular regions to avoid any notable spectral line. A model spectrum is obtained by adding synthetic spectra of Simple Stellar Populations (SSPs) of different ages. Before summing the SSPs, extinction is applied to simulate dust distributed in a uniform screen located in front of the stars. The final synthetic spectrum $F_{\rm mod}$ (model flux) will have the form:

$$F_{\rm mod}(\lambda) = \frac{1}{4\pi d^2} \sum_{i=1}^{N} M_i \; L_i(\lambda) \; 10^{-0.4 \; A(\lambda) \; R_V \; E(B-V)_i}, \tag{5}$$

where the sum is over the number of SSPs used by the code (see subsection 4.2 below), d is the luminosity distance to the galaxy, M_i and $L_i(\lambda)$ are the stellar mass and the spectrum (in luminosity per solar mass units) for the ith SSP, respectively, and the function in the exponent represents the extinction, which depends on $A(\lambda)$ (the adopted extinction law), normalized to the V band, and R_V depends on the extinction curve used. The free parameters used in the fitting are the color excess $E(B-V)_i$ (which is used to parametrize extinction as a function of age), and the mass (or, equivalent, SFR): one value for each SSP age. The first one is because we take selective extinction into account: the younger the stellar population age is, the more likely it is located in a more dusty and extinguished zone of a galaxy (i.e., in the dust of the molecular clouds where they were born). For this reason, generally, dust extinction is higher for younger stellar populations (Poggianti et al., 2001).

`SINOPSIS` assumes that all the stellar populations in a galaxy have the same metallicity value at any age. Then, the code compares the observed spectrum, corrected for extinction from the Milky Way, with synthetic spectra exploring the parameter space to find the best combination of mass and extinction values that reproduces the observed spectrum, i.e., the best fit assessed through the minimization of a goodness function.

It should be noted that, in many cases, good fits are obtained with two or more values of metallicity, but the code chooses the metallicity value for the lower χ^2, which should be interpreted as the metallicity of stars dominating the light in the spectrum. Fritz et al. (2007) made an analysis to roughly simulate chemical evolution, by constructing synthetic spectra with different SFHs and varying the metallicity as a function of stellar age. Results clearly show that using a single metallicity to recover total stellar mass and SFH, does not introduce any bias.

4.2 Stellar ages

The initial set of SSPs contains models for up to 220 different stellar ages for each of the 13 metallicity values. Nevertheless, such a high age resolution both non-practical, when a non-parametric SFH is assumed, and also non-reliable when comparing models with observed data. Well-known degeneracies such as the age-metallicity, age-extinction, and the fact that changes in the spectral features are a logarithmic function of age (i.e., the oldest SSPs are very similar), make it practically impossible to find a unique solution with that degree of precision in age. This is why the age resolution is lowered, by binning the SSPs into 12 final spectra (that we will keep calling SSPs, for the sake of simplicity), proved to be enough to reproduce observed data, as demonstrated by Fritz et al. (2007).

The task of the code is to find the combination of 24 parameters (12 for mass and 12 for extinction) that yields the best fit to the observed spectrum, for each of the four chosen metallicity values. This is done by employing an algorithm that randomly explores the space of parameters, looking for the absolute minimum of χ^2. To this end, the code performs 11 optimizations or model fits in the parameter space, obtaining error bars for mass and extinction. In practice, a bad fit can be due to low-quality spectra for several reasons: low SNR, bad flux calibration, presence of telluric lines, bad

sky subtraction, the object could be a type 1-AGN (the fraction of AGNs in WINGS/OmegaWINGS clusters is $\approx 3\%$; Marziani et al., 2017), or possibly it is a star that was misclassified as a galaxy (for a very few objects).
Even though initially there is already a binning in age, once the best fit is obtained, the solution is far from being unique. Thus, a further binning in age is performed such that the resolution is lowered to four age bins. These were selected by both taking into account the general characteristics of SSPs, and by fitting simulated model spectra. For these four ages the SFR is obtained, and thus the SFH (see subsection 4.4). These four age intervals are listed in Table 2, where the age of the oldest stellar population used is set by the age of the Universe at the cluster redshift where the galaxy belongs (t_u). We did not take into account values lower than 10^{-3} $M_\odot$ yr^{-1} for SFR1, as these values imply a poor sampling of the IMF and hence yield non-physical results. A similar logic applies to other values of the SFRs.

$\mathbf{SFR_i}$	**Age range**	**Age bin**
SFR1	$0 - 19.95$ Myr	19.95 Myr
SFR2	$19.95 - 571.5$ Myr	551.55 Myr
SFR3	$0.5715 - 5.754$ Gyr	5.183 Gyr
SFR4	$5.754 - t_u$ Gyr	Δt_u Gyr

Table 2: Age intervals used in `SINOPSIS` to obtain the SFH. t_u means the age of the Universe at the cluster redshift.

4.3 Stellar masses

Fitting the main features of an aperture integrated optical spectrum, allows us to estimate properties of stellar populations, such as total stellar mass, mass of stars as a function of age, mean metallicity, and dust extinction. K-correction is automatically accounted for `SINOPSIS` as the spectral fits are performed at the galaxies' redshifts, and the total mass values are obtained by rescaling from aperture to total magnitude. In doing so, we are assuming that the color gradient from the aperture to the total magnitude is negligible, as done by other authors (e.g., Kauffmann et al., 2003).
It is worth mentioning that, ideally, one should use spectra that cover the whole galaxy, but this is out of reach for the present survey. Fritz et al. (2011) made a comparison between the $(B-V)$ colors within the fiber aperture and a 5 kpc aperture and found that colors in both apertures are very similar (with a mean difference of $B-V \sim 0.1$ mag), and that the color within 5 kpc aperture represents a good approximation to the total color of the galaxy.
To take into account the possible effect that color gradients might have on the total mass (as opposed to the mass in the fiber spectral aperture) determination, Fritz et al. (2007) computed a correction factor that takes into account the color correction when rescaling the aperture mass to the total mass. We have plotted the distribution of this color correction and verified that it very closely follows a Gaussian distribution peaking at zero, with a standard deviation of 0.08.
Moreover, as will be seen in subsection 5.2, our galaxy sample covers most inclinations and hence, in many cases, galaxy outskirts are included in the aperture spectrum. We observe no trend of total mass or SFR with inclination. Fritz et al. (2011) also made a careful comparison between the masses obtained with `SINOPSIS` and masses from the SDSS (Gallazzi et al., 2005), and obtained a good agreement.

Finally, stellar mass values are taken according to definition 2 in Longhetti and Saracco (2009), which is the mass contained in both stars still in the nuclear burning phase and in remnants (white dwarfs, neutron stars and black holes); hence, stellar mass does not include mass lost due to stellar evolution and supernovae.

4.4 Star formation histories

In subsection 4.2, we mentioned that the code uses 12 SSPs of different ages to search for the best fitting model and that these 12 ages are binned in four intervals as shown in Table 2, with which the SFH is properly recovered (Fritz et al., 2011). The SFR for each of the four age ranges is computed by adding the stellar mass, as defined before, contained in the SSPs that constitute the bin, divided by the combined duration. For calculating the current SFR (in the last $\sim$ 20 Myr, or SFR1), a fit is performed to the EW of the emission lines: Hα, Hβ, and [OII]. These lines are entirely attributed to star formation processes, but other mechanisms like LINERS and AGNs can produce ionizing flux and produce an overestimate of the current SFR. We assume that a low Hα flux (EW $0 <$ H$\alpha < 6\AA$; Sánchez et al., 2014; Cid Fernandes et al., 2013) is not caused by star formation, and hence for these low values we always take the present-day SFR as 0.

4.5 The adopted setup

`SINOPSIS` is a quite flexible code that allows the user to define how the fit is to be performed and many of the parameters. We have fitted 11369 spectra using the setup and parameters that will be described hereafter.

A non–parametric prescription was assumed for the SFHs, meaning that the SFRs are allowed to vary freely and independently for stellar populations of different ages (as opposed to analytical forms). As for the SSP models, the theoretical spectra of Charlot & Bruzual were adopted. These use a Chabrier (2003) IMF with stellar masses between 0.1 and 100 $M_{\odot}$. Nebular emission lines were calculated for the youngest ($t < 50 \times 10^7$ years) SSP, by means of the photoionization code CLOUDY (Ferland, 1996), and assuming physical parameters typical of HII regions (see Fritz et al., 2017, for more details). In this fashion, we are also able to calculate the recent SFR based on Balmer emission line intensity. As for the extinction, we adopt the mean Galactic extinction curve (Cardelli et al., 1989). From 13 possible metallicity values to explore, given in the SSP database, we selected four: sub-solar ($Z = 0.004$), solar ($Z = 0.017$), and super-solar ($Z = 0.03$, 0.04).

As already explained above, `SINOPSIS`, when using non-parametric SFHs, utilizes spectra of 12 different ages. These include four spectra in the age range between 0 and 20 Myr; this is the typical age range in which stars can significantly ionize the gas and hence produce emission lines. To calculate SFR from emission lines, it is usually assumed to be constant over approximately 10^7 years. To be consistent with this approach, we chose to keep the SFR of the four youngest SSP constant as well. This hence reduces the number of parameters to 21 instead of 24.

We also exploited and tested a new feature of the code that was developed specifically for this project, which is the automatic calculation of the oldest SSP to be used in the fit. This is chosen to be the oldest possible SSP, from the full model grid, that is still compatible with the age of the Universe at the galaxy redshift. In this way, we are calculating the stellar mass value more consistently.

5 Physical properties of the sample

5.1 Sample selection

Once in possession of all the measured or calculated observables and physical quantities, we defined the sample of objects to be used in our analysis. Galaxies ending up in the final sample should satisfy the following requirements:

1. Be a cluster member.
2. Have an absolute V magnitude brighter than $M_V = -18.5$ mag, corresponding to a stellar mass limit of approximately $M_* > 3 \times 10^9$ $M_\odot$.
3. Have a good spectral fit from `SINOPSIS`, represented by a valule of $\chi^2 \leq 5$.

The imposed limit in M_V is related to the photometric threshold reached in observations, in which WINGS clusters are complete up to $V = 20.0$. Our limit ($M_V = -18.5$) is in agreement with Guglielmo et al. (2015; $M_B < -18.7$) for the WINGS dataset. Our final sample comprises all 33 OmegaWINGS clusters with spectroscopy, all 22 southern WINGS clusters, while for northern WINGS clusters, we only used 4/22 because of the reasons mentioned above. The final sample from WINGS and OmegaWINGS contains 4349 galaxies (9601 weighted) in 43 clusters.

5.2 Inclination distribution

As mentioned previously, for this work we use aperture spectra, which only cover the central part of galaxies (aperture diameter $\sim 2-3$ kpc), as many other authors have done, finding consistent results (see SDSS, e.g., Kauffmann et al., 2004; and also for WINGS, e.g., Guglielmo et al., 2015; Paccagnella et al., 2016). To review whether the derived SFHs are biased towards stellar populations in the center of galaxies, we have checked the distribution of the inclination of galaxies. We retrieved inclination angles for 672 S0s and 309 spirals of our full sample matched with the HyperLEDA[2] catalog. As can be seen in Figure 1. The pile-up of points with $i = 90°$ can be explained by the fact that it is difficult to precisely measure the inclination of galaxies seen almost edge-on. The fact that the distribution of inclination values is mainly flat and shows no trend with the mass, gives us a good indication that fiber spectra are indeed sampling stellar populations in a whole range of galactocentric distances for the great majority of galaxies.

5.3 SFH as a function of morphological type

Once we had run all the spectra through `SINOPSIS` and defined the final sample, we made several consistency tests to check the reliability of the derived SFHs, and verify whether we could indeed take the results obtained from the analysis of the fiber spectrum as representative of the whole galaxy. We first divided the sample by morphological type, using four categories, as defined in subsection 3.4: ellipticals (E), lenticulars (S0s), early spirals (SpE), and late spirals (SpL, including irregular galaxies); we then calculated the weighted mean of SFR for each type in the four age bins defined above, as shown in Figure 2a. We see that ellipticals are, on average, the most massive galaxies (higher SFR in the two oldest age bins), and there is a clear sequence of SFH as a function of the morphological type. To better visualize the qualitative differences in the SFHs, we normalize SFRs to the oldest value (see Figure 2b). Hereinafter for all the SFHs, the quoted uncertainties on the mean SFRs are estimated as $\sigma/\sqrt{N_{\rm w}}$ (Rider, 1960), where σ is the standard deviation of the weighted distribution, and $N_{\rm w}$ is the weighted number of galaxies.

[2] `http://leda.univ-lyon1.fr/`

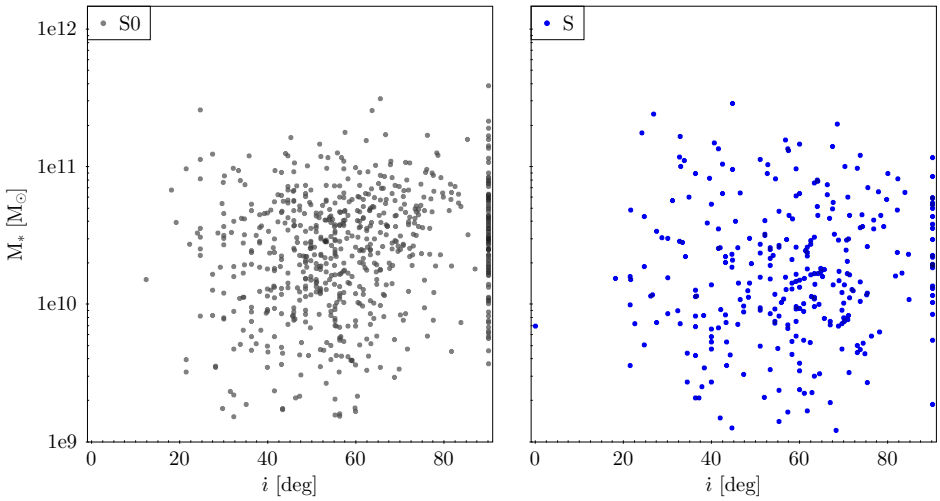

Figure 1: Stellar mass obtained with `SINOPSIS` versus galaxy inclination for S0s (left panel) and spirals (right panel). There is no trend of total stellar mass with inclination angle. Several galaxies are reported as seen edge-on ($i = 90°$).

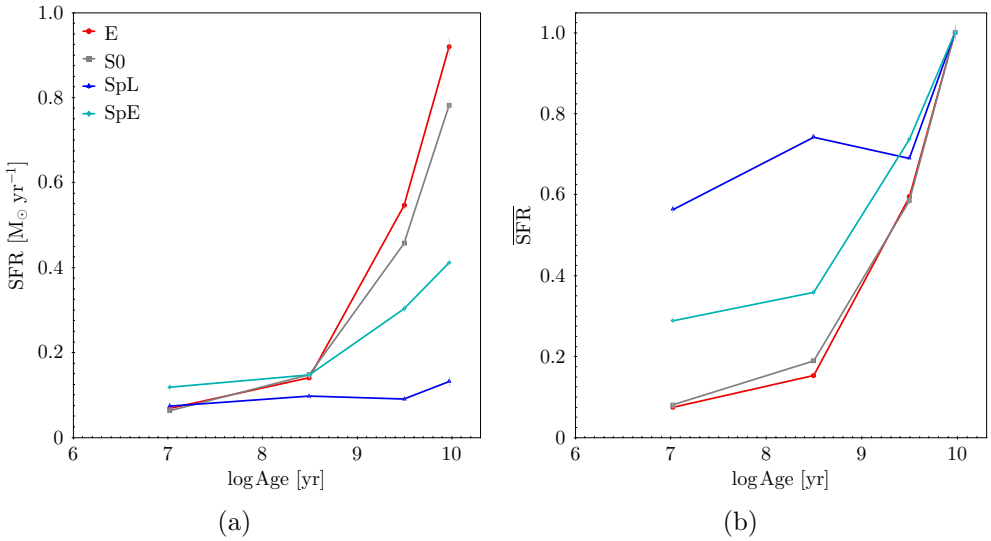

Figure 2: SFHs for the final sample. ***Left:*** For the main galaxy morphological types. ***Right:*** Same SFHs, normalized to the oldest age bin (SFR4). All the results have been corrected for incompleteness.

The SFHs we have recovered from our sample, fit very well in a downsizing scenario (Cowie et al., 1996), from many points of view. We see that the more massive the galaxies are, the steeper their SFR is as a function of cosmic time, as already observed in many other works, e.g., (Brinchmann et al., 2004; Chen, 2009). This is clearly shown later in Figure 6a for spiral galaxies, where a clear monotonic trend is observed at all masses. Furthermore, those trends are reflected in the galaxies' morphology, with early types ones being more massive, and lying on a nice sequence with a 1:1 correspondence between morphological classification and SFH (see Figure 2b). In local clusters, the sSFR is dominated by SpL.

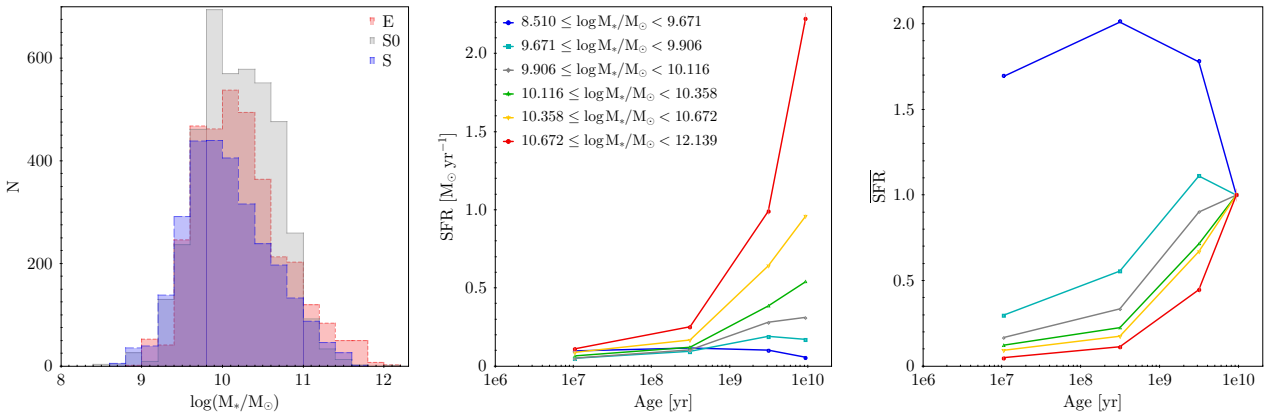

(a) (b) (c)

Figure 3: ***Left:*** Distribution of stellar mass for galaxies divided into the three main morphological types: elliptical (red), lenticulars (gray), and spirals (blue). ***Middle:*** SFH for all galaxies separated in six bins of stellar mass. ***Right:*** The same SFH normalized to the oldest age bin (SFR4). All distributions correspond to final sample, and have been corrected for incompleteness.

5.4 Mass distribution

As defined in subsection 5.1, objects in our final sample of galaxies possess total stellar masses $M_* \gtrsim 3 \times 10^9\ M_\odot$. The sample is complete above this limit, and the distribution of galaxy masses reaches $M_* \sim \times 10^{12}\ M_\odot$, as seen in Figure 3a; this time the galaxies are grouped in only three main morphological types: elliptical, S0, and spirals (including irregulars). On average, ellipticals have higher masses, followed by S0s, and spiral, in that order. Dividing all the galaxies in the final sample into six stellar mass bins (the bins were chosen in such a way that they contain a similar weighted number of galaxies), we have obtained the weighted mean for the SFHs, as shown in Figure 3b. The SFH-mass relation is remarkably well defined and follows a clear trend for galaxies in all mass bins. Figure 3c displays the SFH normalized to the oldest age. Except for the lowest mass bin, the SFR drops rapidly towards recent ages. Conversely, for the lowest mass galaxies, the SFR today is almost two times higher than for the oldest age bin. A possible interpretation of this SFH will be given later on.

6 Results

The goal of the present project is to study the properties of stellar populations of WINGS and OmegaWINGS galaxies as a function of their morphology, galaxy location (projected distance to the cluster center), environment (local density), cluster mass tracers (velocity dispersion and X-ray luminosity), and membership within substructures. This will ultimately give us insights on the quenching mechanisms that are affecting star formation activity in clusters, and on their effectiveness as a function of the cluster (cluster mass, virialization state) and the galaxies' properties (stellar mass, morphology). Furthermore, using a sample of field galaxies drawn from the same survey and a sample of high redshift galaxy clusters, comparisons can be made to highlight evolutionary processes in an unbiased way.

6.1 Fraction of morphological types with cluster properties

One of the main goals of the WINGS survey was to study the fraction of morphological types in nearby clusters as a function of cluster properties: X-ray luminosity, $L_{\rm X}$, and velocity dispersion, $\sigma_{\rm cl}$ (Poggianti et al., 2009). Here, we extend the analysis to the 44 clusters observed in common by both the WINGS and OmegaWINGS surveys including, in this way, galaxies located further away from cluster centers. The galaxy sample is the same described in subsection 3.1, with a luminosity $M_V \leq -18.5$, similar to (Poggianti et al., 2009). In the following, we gather the galaxies in three broad morphological classes: ellipticals (E), lenticulars (S0s), and spirals (S; including all galaxies later than S0s).

Figure 4 shows the fractions of morphological types as a function of cluster velocity dispersion. The solid lines are the least-square fits, which are practically flat, with a weak correlation coefficient[3] of 0.20 for ellipticals, and moderate correlations of 0.46 and -0.42 for S0s and spirals, respectively. The morphological trends as a function of X-ray luminosity are shown in Figure 5, together with the least-square fits. This time we find moderate correlations for the three morphological classes: 0.48 for ellipticals, 0.49 for S0s, and -0.62 for spirals. Taking into account the Poisson error bars in the fractions, these results indicate that there may be a correlation between the three fraction types and $L_{\rm X}$, and between the S0 and spiral fractions with $\sigma_{\rm cl}$. While elliptical and S0 fractions increase with cluster mass, the opposite is true for spirals.

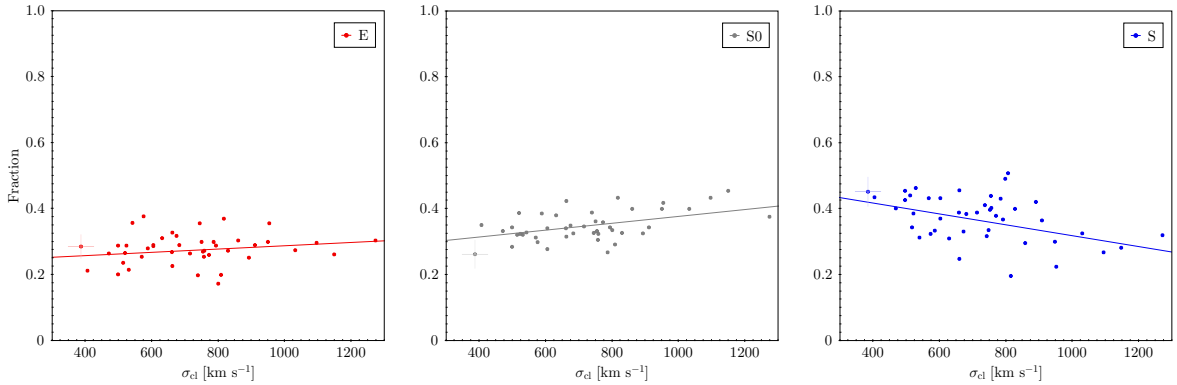

Figure 4: Fraction of galaxy morphological types in both the WINGS and OmegaWINGS datasets, as a function of cluster velocity dispersion ($\sigma_{\rm cl}$): ellipticals (left), S0s (middle), and spirals (right). Mean Poisson errors are shown for the first point in each panel, while the horizontal error bar is the average of the cluster velocity dispersion errors. The least-square fit is shown in each panel.

On average, the fractions of morphological types in clusters are: $27.9 \pm 3.7\%$ for ellipticals, $38.8 \pm 4.3\%$ for S0s, and $37.3 \pm 4.5\%$ for spirals. In comparison with the fractions obtained by Poggianti et al. (2009) (only for WINGS galaxies, i.e., galaxies within $0.6 \times R_{200}$), our fraction of spiral galaxies is higher at the expense of a lower elliptical fraction, while the S0 fraction remains more or less unchanged. We attribute these results to our inclusion of galaxies in clusters outskirts, and hence to the morphological evolution that spiral galaxies experiment as they are falling towards the cluster centers. In this process, they suffer interactions both with the intracluster gas and other galaxies, and are transformed into earlier types (e.g., Boselli and Gavazzi, 2006; Cava et al., 2017).

[3]The Pearson's correlation coefficient is a measure of the statistical relation between two variables. It gives information about the magnitude of association, and the direction of the relation.

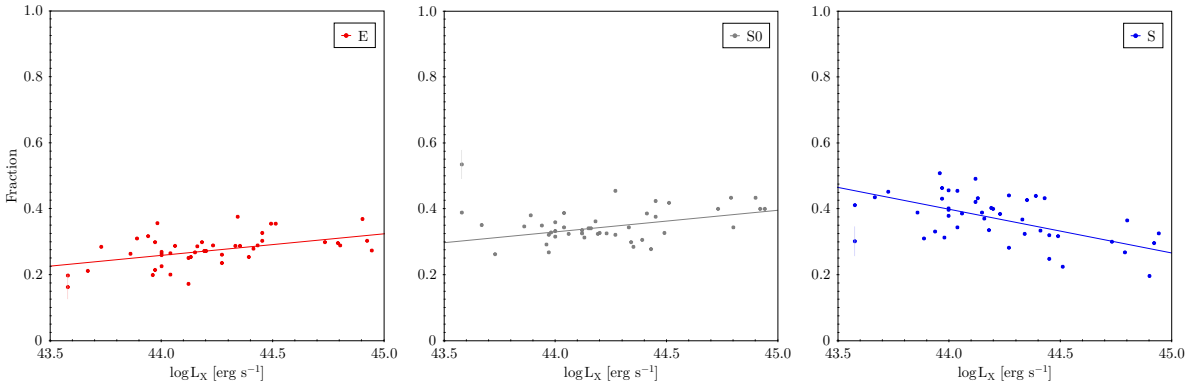

Figure 5: Fraction of galaxies in both WINGS and OmegaWINGS datasets, as a function of cluster X-ray luminosity (L_X). Mean Poisson errors are shown in each first point. The least-square fit is shown in each panel.

6.2 SFH for spiral galaxies

The central part of this work is focused on the analysis of SFH of spiral galaxies. Spirals are of crucial importance in this context, as they are the galaxies most affected by the cluster environment. They undergo transformations in both their morphology and stellar content, evolve differently from their isolated counterparts. The latter are basically undergoing secular evolution, strongly dominated by internal processes (see subsection 1.1), while cluster spirals are also subject to a much wider variety of interaction mechanisms, whose efficiency depends both on the cluster and on the galaxy properties. We aim to answer questions such as: What kind of spiral galaxies are in each group? Very late or earlier types? Where are these galaxies located? What are their velocities? In essence: Where do these galaxies come from? Have they been in the cluster for a long time or were they recently accreted?

6.2.1 SFH and stellar mass

The SFR-mass relation has been widely studied in the field, with a few works devoted to clusters (e.g., Paccagnella et al., 2016). Several studies (e.g., Wijesinghe et al., 2012) have failed to find a relation between local density, SFR, and mass. Here we study the SFR for spirals, divided into four mass bins (see Figure 6), each one with a weighted number of ~ 710 galaxies. Figure 6b shows the same SFH, normalized to the oldest age bin (SFR4). The SFR-mass relation for spirals is fulfilled, for all ages and in particular for stellar masses $M_* > 10^{10}$ M$_\odot$.
We also observe, from Figure 6b, that very low-mass spirals ($\log M_*/M_\odot \lesssim 9.7$) have a higher star formation activity through most of their life, compared to the SFR at the oldest ages. On average, the correlation between stellar mass and morphology still holds when considering only spirals: lower-mass spirals tend to display later morphological type vis-a-vis more massive ones. This result confirms downsizing in a complete, homogeneous way, in clusters. We should not forget that, on top of the downsizing phenomenology, we are also observing the effect of the interaction between the galaxies and the cluster environment. Spirals in clusters are very likely dominated by infalling galaxies that will feed the S0 populations; the latter will dominate this environment, through morphological transformations, in a timescale of about 1-3 Gyr (Kodama and Smail, 2001; Bekki et al., 2002). Now, it has been proposed that the mechanisms driving changes in spiral

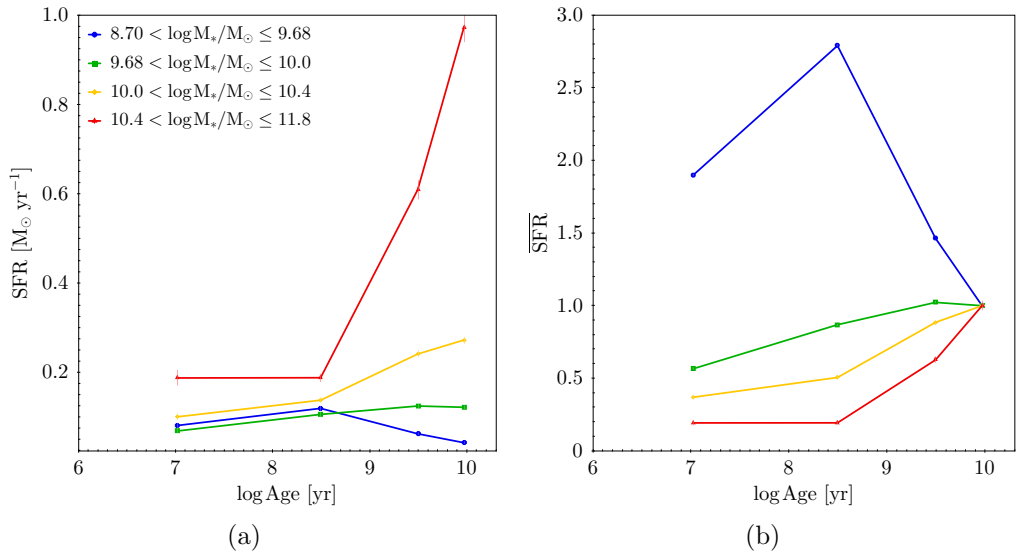

(a) (b)

Figure 6: ***Left:*** SFH for spiral galaxies in the final sample, divided into four bins of total stellar mass. ***Right:*** The same SFH normalized to the oldest age bin. All the results have been corrected for incompleteness.

galaxies might depend not only on the cluster properties, but also on the galaxy stellar mass. Fraser-McKelvie et al. (2018a) investigated the quenching mechanism of a sample of 35 low-redshift spiral galaxies, and concluded star formation is suppressed by different mechanisms that depend on galaxy mass. Low mass (i.e. $M \lesssim 10^{10}$ $M_{\odot}$) spirals are likely quenched by hydrodynamical interactions (such as ram-pressure stripping or starvation) acting on relatively short timescales. High-mass galaxies are probably affected by multiple mechanisms; these might be due to internal and external nature.

Now, while galaxies in the two most massive bins display typically declining SFHs, those in the less massive bins have quite flat or even increasing SFR as a function of time. Such patterns in the SFR have been observed in jellyfish galaxies of the GAs Stripping Phenomena in galaxies with MUSE (GASP; Poggianti et al., 2017) sample. Numerical simulations of galaxies in-falling in clusters predict that, when a galaxy moves within the ICM, the pressure exerted by the latter on the interstellar medium results in an increase of its density which, in turn, will trigger an episode of star formation (Kronberger et al., 2008; Steinhauser et al., 2016; Köppen et al., 2018). Gaspar-Gorostieta (Master Thesis, 2020), using MUSE integral field data to study ram pressure-induced SFR in a sample of 64 galaxies with clear evidence of such interaction, found that the intensity of this burst has a strong, clear dependence on the galaxy mass: the higher the total mass, the lower the enhancement. Furthermore, the enhancement is more evident in the second age bin (actually representing a longer age range, while the current SFR is based on an almost instantaneous measurement), as we observe here. This might be considered as a strong proof of ram pressure acting to first enhance and then quench star formation. Hence, we are confirming that quenching in low-mass spirals is mainly driven by hydrodynamic mechanisms, namely ram-pressure stripping. For higher-mass galaxies, the issue remains more uncertain, since ram pressure does not seem to leave a signature as strong as in low mass ones. A more careful analysis, maybe involving finer age bins and comparison with field galaxies, may clarify this issue.

6.2.2 SFH and projected radial distance

At least for spirals, we expect that galaxies located at larger clustercentric projected distances have on average a higher SFR. This is because these galaxies should be still unperturbed or in the first phase of their interaction with the cluster, and their properties not yet affected by the environment. This is indeed what we can note in Figure 7, for spirals separated in six bins of projected radial distance, each one with a weighted number of $\sim$ 567 galaxies. There is a clear trend of SFR with projected distance, although not at older ages. Galaxies located at the cluster outskirts are expected to be rich in gas, with a high SFR, and they eventually lose their gas through the different mechanisms mentioned in subsection 1.1.

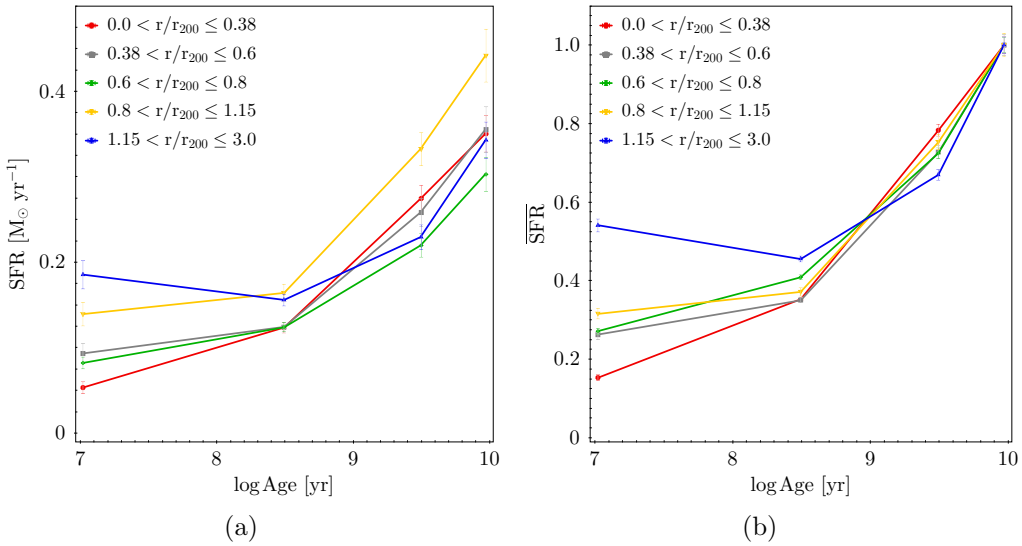

Figure 7: ***Left:*** SFHs for spiral and irregular galaxies in the final sample. ***Right:*** Same SFHs normalized to the oldest age bin (SFR4). All the results have been corrected for incompleteness.

Furthermore, from our results, there is no evident trend of mass versus projected radius (as expected). So overall, we can confidently conclude that we are observing a clear clustercentric distance effect, although the distance is a projected value. As we consider galaxies further away from the center of the cluster, they are less contaminated by galaxies that are close only in projection, making the result even stronger. It would also be tempting to interpret the raising SFR of the farther (from the center) galaxies as an effect of ram pressure (see Subsec. 6.2.1), happening as the galaxies start interacting with the ICM. A more careful look will be given to these galaxies to better understand their nature: these might be objects that will eventually develop jellyfish morphologies.

6.2.3 SFH and local density

There is a well-known relation between the local density of a galaxy, i.e., the number of galaxies within a certain projected distance, and the morphology: the so-called morphology-density relation (Dressler, 1980). Cluster members of WINGS/OmegaWINGS follow this relation quite well (plot not shown). However, a relation between SFR and local density has not been clearly found yet. Tyler et al. (2013) studied cluster and field galaxies without finding any difference in the SFR distribution of both groups in relation to local density. Analyzing the existence of a possible relation between SFR (or, more in general, SFH) and local density might provide insights on the mechanisms affecting stellar populations: is it the influence of the cluster in general, or is it the

higher density of galaxies? Of course, local density is a function of the clustercentric distance: the closer to the cluster center, the higher the number of galaxies per unit area will be (plot not shown), so that disentangling the two effects is not straightforward.

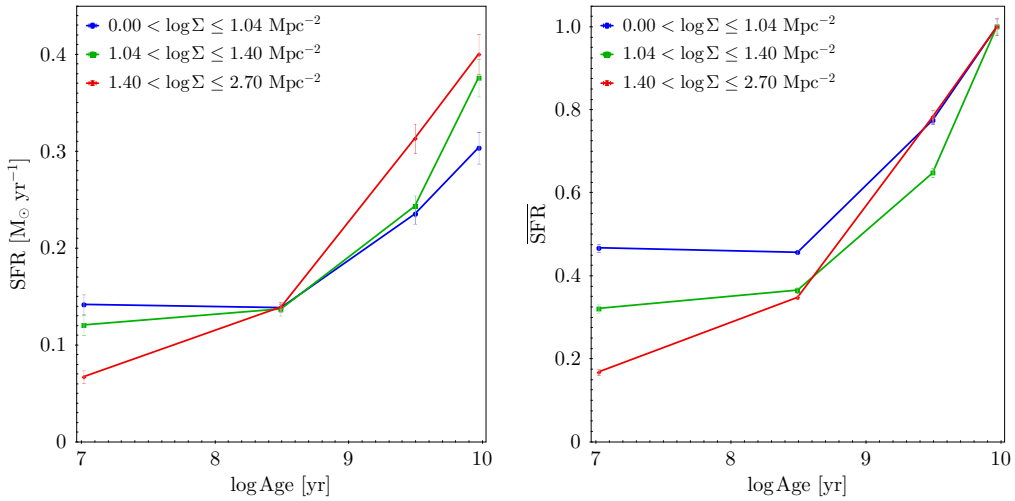

Figure 8: ***Left:*** SFHs for spiral and irregular galaxies in the final sample, divided into three groups of local density. ***Right:*** Same SFHs, normalized to the oldest age bin (SFR4). All the results have been corrected for incompleteness.

Here, we study the SFH dividing our spiral sample into three local density bins (see Figure 8), each one with a weighted number of $\sim$ 950 galaxies. We see that spirals located in low density environments (i.e., cluster outskirts) have a higher SFR today than those galaxies in more dense areas, as expected. We need to keep in mind, though, that spirals, and even more very late spirals, are very scarce at small clustercentric distances. On the other hand, beyond present-day SFR, it is still unclear how the SFH changes with local density values.

6.2.4 SFH and cluster properties

As seen in subsection 6.1, the fractions of different morphological types change with cluster mass tracers, in particular for spiral galaxies. We have investigated if the global environment, parameterized by the clusters' velocity dispersion and X-ray luminosity, affects the SFH as well. We do not see any relation between these cluster properties and neither the SFH nor the present-day SFR (plots not shown). The fact that the average SFR of spirals does not depend on the cluster mass might seem surprising, but it is not a completely new finding: both Poggianti et al. (2006) and Fritz et al. (2014) find that the fraction of emission-line galaxies does not depend on the cluster mass. Here, we not only confirm this result by extending it to a wider cluster area and a larger number of galaxies, but we also directly relate it to the average SFR (instead of the simple emission line detection).

7 Summary and future work

We take advantage of the large dataset described above to identify relations between several clusters in the local universe and galaxy properties, in order to gain physical insights on the mechanisms

that transform spiral galaxies when they are accreted into clusters, on what those mechanisms are, and how they act. Our analysis exploits stellar population synthesis techniques applied to optical spectra, with the aim to gather information about the stellar content of galaxies. Other properties, characterizing the environment, as used as well. We can summarize our results as follows:

1. Even though the SFHs are derived by analyzing spectra from the inner regions of galaxies, their characteristics very well match the ones expected for given morphological type.

2. We believe that lower-mass spirals show signatures of the double effect of ram pressure, firstly enhancing the SFR as the galaxy experiences its first contact with the ICM, and then quenching star formation when the gas is stripped. This is consistent with the behavior observed in a sample of bona fide ram pressure influenced galaxies.

3. Spirals of higher mass do not show this SFH signature typical of a ram-pressure effect. More than one mechanism can be acting in their case, and this needs to be thoroughly investigated.

4. Projected location is likely to play a major role in halting star formation: galaxies in the outskirts display higher SFR (and sSFR), compared to galaxies found at the cluster center, with the average SFR almost monotonically decreasing for diminishing distances.

5. It is not completely clear whether the above is a local effect, due to the higher density of galaxies in the innermost cluster regions (hence increasing the interaction probability by, e.g., harassment), or a global one.

6. We confirm the previous finding that the mass of the cluster is not what drives quenching. Instead, ram-pressure stripping is a very likely mechanism to quench star formation, as it is found to act very efficiently also in low-mass clusters (see, e.g., Poggianti et al., 2017).

The next step of this work involves the comparison of stellar population properties of cluster spirals with their counterparts in lower density environments. The sample will be drawn from the non-members sample of WINGS/OmegaWINGS, ideal for such kind of comparison. Furthermore, we will explore the reliability of the results obtained by adopting a higher SSP age resolution. This was already quite successfully attempted by Guglielmo et al. (2015), and might help to disentangle the effects of different quenching processes.
In the forthcoming part of this project, we also aim to explain the correlations already found through physical processes driving galaxy evolution in clusters, in particular those fueling the conversion of spirals into S0s. Afterwards, with the purpose of comparing our results at low redshift with intermediate-high redshift data, we will apply the same analysis techniques to the ESO Distant Clusters Survey (EDisCS[4]; Milvang-Jensen et al., 2008; Desai et al., 2007) with 20 clusters at $0.5 < z < 0.8$, and the MORPHS[5] dataset (Dressler et al., 1999), with 11 clusters at $0.37 < z < 0.56$. Our ultimate goal is to perform a complete study of galaxy evolution in clusters and in the field, from the nearby to the more distant Universe.

[4] `https://www.mpa.mpa-garching.mpg.de/galform/ediscs/`
[5] `http://star-www.dur.ac.uk/~irs/morphs.html`

References

Baldry, I. K., Balogh, M. L., Bower, R., Glazebrook, K., et al. (2004). In Allen, R. E., Nanopoulos, D. V., and Pope, C. N., editors, *AIPC*, volume 743 of *American Institute of Physics Conference Series*, pages 106–119.

Beers, T. C., Flynn, K., and Gebhardt, K. (1990). *AJ*, 100:32.

Bekki, K., Couch, W. J., and Shioya, Y. (2002). *ApJ*, 577:651–657.

Bertin, E. and Arnouts, S. (1996). *AAPS*, 117:393.

Biviano, A., Moretti, A., Paccagnella, A., et al. (2017). *AAP*, 607:A81.

Boselli, A. and Gavazzi, G. (2006). *PASP*, 118, 517.

Brinchmann, J., Charlot, S., White, S. D. M., Tremonti, C., et al. (2004). . *MNRAS*, 351:1151–1179.

Bundy, K., Bershady, M. A., Law, D. R., Yan, R., et al. (2015). *ApJ*, 798:7.

Burrows, A. (2000). *Natur*, 403:727–733.

Butcher, H. and Oemler, A., J. (1978). *ApJ*, 226:559–565.

Butcher, H. and Oemler, A., J. (1984). *ApJ*, 285:426–438.

Byrd, G. and Valtonen, M. (1990). *ApJ*, 350:89.

Cardelli, J. A., Clayton, G. C., and Mathis, J. S. (1989). *ApJ*, 345:245.

Cava, A., Bettoni, D., Poggianti, B. M., Couch, W. J., et al. (2009). *A&A*, 495:707–719.

Cava, A., Biviano, A., Mamon, G. A., et al. (2017). *A&A*, 606, 108.

Chabrier, G. (2003). *PASP*, 115:763–795.

Chen, Y. M. (2009). In Heinz, S. and Wilcots, E., editors, *AIPC*, volume 1201 of *American Institute of Physics Conference Series*, pages 45–48.

Cid Fernandes, R., Pérez, E., García Benito, R., González Delgado, R. M., et al. (2013). *A&A*, 557:A86.

Colless, M., Dalton, G., Maddox, S., Sutherland , W., et al. (2001). *MNRAS*, 328:1039–1063.

Contini, E., Gu, Q., Kang, X., et al. (2019). *ApJ*, 882:167.

Cowie, L. L. and Songaila, A. (1977). *Natur*, 266:501–503.

Cowie, L. L., Songaila, A., Hu, E. M., and Cohen, J. G. (1996). *AJ*, 112:839.

Debattista, V. P. and Sellwood, J. A. (2000). *ApJ*, 543:704–721.

Desai, V., Dalcanton, J., Aragon-Salamanca, A., et al. (2007). *A&A*, 660, 1151.

Dressler, A. (1980). *ApJ*, 236, 351.

Dressler, A., Smail, I., Poggianti, B., et al. (1999). *ApJS*, 122-51.

Ebeling, H., Edge, A. C., Allen, S. W., Crawford, C. S., et al. (2000). *MNRAS*, 318:333–340.

Ebeling, H., Edge, A. C., Bohringer, H., Allen, S. W., et al. (1998). 301:881–914.

Ebeling, H., Voges, W., Bohringer, H., Edge, A. C., et al. (1996). *MNRAS*, 281:799–829.

Fasano, G., Marmo, C., Varela, J., et al. (2006). *A&A*, 445, 805.

Fasano, G., Vanzella, G., Dressler, A., et al. (2012). *MNRAS*, 420, 926.

Ferland, G. J. (1996). *Hazy, A Brief Introduction to Cloudy 90*.

Fraser-McKelvie, A., Aragón-Salamanca, A., et al. (2018a). *MNRAS*, 481:5580.

Fraser-McKelvie, A., Brown, M. J. I., et al. (2018b). *MNRAS*, 474:1909.

Fritz, J., Moretti, A., Gullieuszik, M., Poggianti, B., et al. (2017). *ApJ*, 848:132.

Fritz, J., Poggianti, B., Cava, A., et al. (2007). *A&A*, 470, 137.

Fritz, J., Poggianti, B., Cava, A., et al. (2011). *A&A*, 566, A32.

Fritz, J., Poggianti, B. M., Cava, A., Moretti, A., et al. (2014). *A&A*, 566:A32.

Gallazzi, A., Charlot, S., Brinchmann, J., White, S. D. M., et al. (2005). *MNRAS*, 362:41–58.

Guglielmo, V., Poggianti, B. M., Moretti, A., Fritz, J., et al. (2015). *MNRAS*, 450:2749–2763.

Gullieuszik, M., Poggianti, B., Fasano, G., et al. (2015). *MNRAS*, 581, A41.

Gunn, J. E. and Gott, J. Richard, I. (1972). *ApJ*, 176:1.

Kauffmann, G., Heckman, T. M., White, S. D. M., Charlot, S., et al. (2003). *MNRAS*, 341:33–53.

Kauffmann, G., White, S. D. M., Heckman, T. M., Ménard, B., et al. (2004). *MNRAS*, 353:713–731.

Kennicutt, Robert C., J. (1998). *ARA&A*, 36:189–232.

Kodama, T. and Smail, I. (2001). *MNRAS*, 326(2):637–642.

Köppen, J., Jáchym, P., Taylor, R., and Palouš, J. (2018). *MNRAS*, 479:4367–4390.

Kronberger, T., Kapferer, W., Ferrari, C., Unterguggenberger, S., et al. (2008). *AA*, 481:337–343.

Larson, R. B., Tinsley, B. M., and Caldwell, C. N. (1980). *ApJ*, 237:692–707.

Liu, C., Hao, L., Wang, H., and Yang, X. (2019). *arXiv:1905.11008*.

Liu, C.-X., Pan, D. C., Hao, L., Hoyle, F., et al. (2015). *ApJ*, page 165.

Longhetti, M. and Saracco, P. (2009). *MNRAS*, 394:774–794.

Marziani, P., D'Onofrio, M., Bettoni, D., Poggianti, B. M., et al. (2017). *AA*, 599:A83.

Milvang-Jensen, B., Noll, S., Halliday, C., et al. (2008). *A&A*, 482, 419.

Moore, B., Katz, N., Lake, G., Dressler, A., et al. (1996). *Natur*, 379:613–616.

Moretti, A., Gullieuszik, M., Poggianti, B., et al. (2017). *A&A*, 599, A81.

Paccagnella, A., Vulcani, B., Poggianti, B. M., Moretti, A., et al. (2016). *ApJL*, 816:L25.

Peebles, P. J. E. (1993). *Principles of Physical Cosmology*. Princeton Univ. Press, Princeton, NJ.

Poggianti, B. M., Bressan, A., and Franceschini, A. (2001). *ApJ*, 550:195–203.

Poggianti, B. M., Fasano, G., Bettoni, D., et al. (2009). *ApJL*, 697:L137.

Poggianti, B. M., Moretti, A., Gullieuszik, M., Fritz, J., et al. (2017). *ApJ*, 844:48.

Poggianti, B. M., von der Linden, A., De Lucia, G., et al. (2006). *ApJ*, 642:188.

Postman, M., Franx, M., Cross, N. J. G., Holden, B., et al. (2005). *ApJ*, 623:721–741.

Rider, P. R. (1960). *JASA*, 55:148–150.

Sánchez, S. F., Rosales-Ortega, F. F., Iglesias-Páramo, J., Mollá, M., et al. (2014). *AA*, 563:A49.

Schawinski, K., Urry, C. M., Simmons, B. D., Fortson, L., et al. (2014). *MNRAS*, 440:889–907.

Silk, J. and Rees, M. J. (1998). *A&A*, 331:L1–L4.

Smethurst, R. J., Lintott, C. J., Simmons, B. D., Schawinski, K., et al. (2015). 450:435–453.

Steinhauser, D., Schindler, S., and Springel, V. (2016). *A&A*, 591:A51.

Strauss, M. A., Weinberg, D. H., Lupton, R. H., Narayanan, V. K., et al. (2002). *AJ*, 124:1810–1824.

Toomre, A. (1977). In Tinsley, B. M. and Larson, Richard B. Gehret, D. C., editors, *egsp.conf*, page 401.

Tyler, K. D., Rieke, G. H., and Bai, L. (2013). *ApJ*, 773:86.

Varela, J., D'Onofrio, M., Marmo, C., Fasano, G., et al. (2009). *A&A*, 497:667.

Vulcani, B., Poggianti, B. M., Fasano, G., Desai, V., et al. (2012). *MNRAS*, 420:1481.

Wijesinghe, D. B., Hopkins, A. M., Brough, S., Taylor, E. N., et al. (2012). *MNRAS*, 423:3679–3691.

Wuyts, S., Förster Schreiber, N. M., van der Wel, A., Magnelli, B., et al. (2011). *ApJ*, 742:96.

A Appendix

The WINGS cluster sample defined in section 2 is shown in Table 3 with some basic properties: mean redshift (z), velocity dispersion ($\sigma_{\rm cl}$) obtained from the data themselves, virial radius (R_{200}), and X-ray luminosity (L_X) from the ROSAT All-Sky Survey. The WINGS-SPE and OmegaWINGS-SPE columns in the table indicate if that cluster has spectroscopic observations, and the last column shows whether the signal-to-noise ratio of the spectra is sufficient to run the `SINOPSIS` code (see section 4) for that cluster.

Table 3: WINGS cluster sample.

Cluster	z	$\sigma_{\rm cl}$ [km s^{-1}]	R_{200} [Mpc]	$\log L_X$ [erg s^{-1}]	**WINGS-SPE**	**OmegaWINGS-SPE**	**SINOPSIS**
A1069	0.06528	542	1.180	43.98	✓	✓	✓
A119	0.04436	952	2.250	44.51	✓		✓
A1291	0.05090	413	0.860	43.64	✓		
A133	0.06030	623	1.292	44.55			
A147	0.04470	387	0.808	43.73			
A151	0.05327	771	1.670	44.00	✓	✓	✓
A160	0.04317	738	1.600	43.58	✓		
A1631a	0.04644	715	1.390	43.86	✓	✓	✓
A1644	0.04691	945	1.890	44.55	✓		✓
A1668	0.06340	654	1.354	44.20			
A168	0.04518	498	0.970	44.04		✓	✓
A1736	0.04610	918	1.916	44.37			
A1795	0.06291	731	1.720	45.05	✓		
A1831	0.06340	444	0.919	44.28	✓		
A193	0.04852	758	1.580	44.19	✓	✓	✓
A1983	0.04517	407	0.950	44.67	✓		
A1991	0.05860	570	1.330	44.13	✓		
A2107	0.04166	519	1.150	44.04	✓		
A2124	0.06692	733	1.090	44.13	✓		
A2149	0.06750	459	0.948	43.92			
A2169	0.05780	524	1.088	43.65	✓		
A2256	0.05810	1376	2.856	44.85			
A2271	0.05840	460	0.955	43.81			
A2382	0.06442	807	1.730	43.96	✓	✓	✓
A2399	0.05793	662	1.550	44.00	✓	✓	✓
A2415	0.05791	683	1.190	44.23	✓	✓	✓
A2457	0.05889	605	1.310	44.16	✓	✓	✓
A2572a	0.03900	546	1.144	44.01	✓		✓
A2589	0.04217	1147	2.750	44.27	✓		
A2593	0.04188	523	1.210	44.06	✓		
A2622	0.06100	732	1.517	44.03	✓		
A2626	0.05509	650	1.480	44.29	✓		✓
A2657	0.04000	829	1.735	44.2			
A2665	0.05620						
A2717	0.04989	470	1.170	44.00		✓	✓
A2734	0.06147	588	1.380	44.41		✓	✓
A311	0.06570						
A3128	0.06033	793	1.580	44.33	✓	✓	✓
A3158	0.05947	948	1.940	44.73	✓	✓	✓
A3164	0.06110	991	2.054				
A3266	0.05915	1095	2.310	44.79	✓	✓	✓
A3376	0.04652	756	1.650	44.39	✓	✓	✓
A3395	0.05103	1272	2.760	44.45	✓	✓	✓

Continued on next page.

Table 3 – *Continued from previous page.*

Cluster	z	$\sigma_{\rm cl}$	R_{200}	$\log L_X$	WINGS	OmegaWINGS	SINOPSIS
A3490	0.06880	660	1.363	44.24	✓		✓
A3497	0.06800	724	1.496	44.16	✓		✓
A3528a	0.05441	891	1.880	44.12		✓	✓
A3528b	0.05350			44.30			
A3530	0.05480	674	1.401	43.94		✓	✓
A3532	0.05536	662	1.550	44.45		✓	✓
A3556	0.04796	531	1.100	43.97	✓	✓	✓
A3558	0.04829	910	1.950	44.80		✓	✓
A3560	0.04917	799	1.790	44.12	✓	✓	✓
A3667	0.05528	1031	2.220	44.94		✓	✓
A3716	0.04599	753	1.720	44.00		✓	✓
A376	0.04752	832	1.660	44.14	✓		✓
A3809	0.06245	499	1.040	44.35	✓	✓	✓
A3880	0.05794	514	1.200	44.27		✓	✓
A4059	0.04877	744	1.580	44.49		✓	✓
A500	0.06802	660	1.800	44.15	✓	✓	✓
A548b	0.04410	842	1.759	43.48			
A602	0.06210	834	1.728	44.05			
A671	0.04939	730	1.490	43.95	✓		
A754	0.05445	816	1.660	44.90	✓	✓	✓
A780	0.05650			44.82			
A85	0.05568	859	2.020	44.92		✓	✓
A957x	0.04496	631	1.420	43.89	✓	✓	✓
A970	0.05872	749	1.630	44.18	✓	✓	✓
IIZW108	0.04889	575	1.199	44.34	✓	✓	✓
MKW3s	0.04470	604	1.580	44.43	✓		
Rx0058	0.04840	696	1.451	43.64	✓		✓
Rx1022	0.05480	582	1.210	43.54	✓		
Rx1740	0.04410	540	1.128	43.7	✓		
Z1261	0.06440						
Z2844	0.05027	425	0.880	43.76	✓		
Z8338	0.04953	658	1.350	43.9	✓		✓
Z8852	0.04077	786	1.630	43.97	✓		✓